frontiers | Frontiers in Earth Science

TYPE Original Research
PUBLISHED 14 March 2023
DOI 10.3389/feart.2023.1108655

OPEN ACCESS

EDITED BY
Qiuming Pei,
Southwest Jiaotong University, China

REVIEWED BY
Jie Zhou,
Ocean University of China, China
Yingjie Li,
Hebei GEO University, China

*CORRESPONDENCE
Zhibo Liu,
geoleo@163.com
Nan Wang,
wangnan_0912@sina.com

SPECIALTY SECTION
This article was submitted to Structural Geology and Tectonics, a section of the journal Frontiers in Earth Science

RECEIVED 26 November 2022
ACCEPTED 28 February 2023
PUBLISHED 14 March 2023

CITATION
Chen W, Liu Z, Wang N, Wang G, Zheng M, Han N, Hu Y and Yan X (2023), Early cretaceous bimodal volcanic rocks in Wuga Co area, central tibet: The first identification of direct products derived from slab sinking in the Bangong-Nujiang suture zone.
Front. Earth Sci. 11:1108655.
doi: 10.3389/feart.2023.1108655

Early cretaceous bimodal volcanic rocks in Wuga Co area, central tibet: The first identification of direct products derived from slab sinking in the Bangong-Nujiang suture zone

Wei Chen[1], Zhibo Liu[2]*, Nan Wang[2]*, Genhou Wang[1], Ming Zheng[3], Ning Han[1], Yiling Hu[4] and Xukun Yan[1]

[1]School of Earth Science and Resources, China University of Geosciences, Beijing, China, [2]Institute of Mineral Resources, Chinese Academy of Geological Sciences, Beijing, China, [3]QingHai Salt Lake Industry Co., Ltd., Beijing, China, [4]State Key Laboratory of Oil and Gas Reservoir Geology and Exploitation, Chengdu University of Technology, Chengdu, China

Introduction: The Bangong-Nujiang Suture Zone (BNSZ) in central Tibet is a remnant of the Bangong-Nujiang Ocean that records its entire Wilson Cycle. The model of divergent double-sided subduction (DDS) is crucial for elucidating the evolution of tectonomagmatic activity on both sides of the BNSZ and for understanding why no high-pressure metamorphic rocks occur in the BNSZ. However, the DDS geodynamics remain poorly constrained. In particular, there is a lack of reports on magmatic rocks directly associated with slab sinking in the DDS terminal stage.

Methods: This study presents new geochronological, geochemical, and isotopic data for the Early Cretaceous bimodal volcanic rocks around the Wuga Co area.

Results: The bimodal volcanic rocks are divided into the Wuga Co rhyolites (SiO_2 = 77.0–79.0 wt%) and the Wuga Co basaltic andesites (SiO_2 = 53.9–55.5 wt%). The isotopic values of the Wuga Co basaltic andesites with low $(^{87}Sr/^{86}Sr)_i$ values (+0.7040 to +0.7044) and high εNd(t) values (+3.8 to +4.1) lie among three endmembers (the BNO sediments in accretionary wedge, depleted mantle and the BNO slab).

Discussion: These values indicate the partial melting of a mantle peridotite that interacted with the subducted slab and sediment in the accretionary wedge, which was caused by the sinking of the Bangong-Nujiang oceanic slab. The Wuga Co rhyolites (108 Ma) have low $(^{87}Sr/^{86}Sr)_i$ values (+0.703 to +0.706), high εNd(t) values (+2.25 to +2.49), and high εHf(t) values (+5.6 to +10.0). These values indicate that the rhyolite formed by partial melting of juvenile basaltic crust. This study also collected Hf isotope data from both sides of the BNSZ to constrain its evolution. Our results show that the εHf(t) values of magma on both sides of the BNSZ were elevated simultaneously at 130 Ma, which may be caused by the Bangong-Nujiang oceanic slab rupture. Based on these new data, we propose that the Bangong-Nujiang oceanic slab ruptured from the two overlying terranes at approximately 130 Ma and subsequently sank into the mantle at approximately 108 Ma.

KEYWORDS

bangong-nujiang collision zone, bimodal volcanic rocks, divergent double subduction, slab sinking, tibet

1 Introduction

Continent–continent hard collisions in single-sided subduction zones such as the Himalayan and Dabie-Sulu belts create suture zones (Luo A. B. et al., 2022a), resulting connection between the passive continental margins on one side and active continental margin on the other side (Yin and Harrison, 2000; Luo A-B. et al., 2022b). As oceanic lithosphere is consumed by subduction, collision leads to the thickening of the continental crust and the formation of high-pressure metamorphism, such as blue-schist facies. However, there are many suture zones globally where the blue-schist facies is not present, such as the Precambrian Jiangnan Orogen in South China (Zhao, 2015), the Early Paleozoic Lachlan fold belt of southeastern Australia (Soesoo et al., 1997), or the Late Paleozoic-Mesozoic Xing'an-Mongolia Suture Zone in the Central Asian Orogenic Belt (Pei et al., 2018). Soesoo et al. (1997) first elaborated the process of arc-arc soft collisional development caused by divergent double-sided subduction (DDS) to explain the Lachlan Belt in eastern Australia, where high-pressure metamorphism is absent. Therefore, different subduction models result in different collision forms. Single-sided subduction eventually leads to continent-continent hard collisions and DDS leads to arc-arc soft collisions. Analyzing the geochemical characteristics of these igneous rocks is essential to understand the subduction form and the collisional model it causes.

The Bangong-Nujiang Suture Zone (BNSZ) is a remnant of the Meso-Tethys Ocean and an important tectonic belt sandwiched between the southern Qiangtang Terrane and the Lhasa Terrane in the central Tibetan Plateau (Allégre et al., 1984; Girardeau et al., 1984; Yin and Harrison, 2000; Zhu et al., 2013). However, the subduction polarity of the Bangong-Nujiang Ocean (BNO) and the collisional model caused by it is still a matter of debate (Zhang et al., 2021; Guo et al., 2022; Hu X. et al., 2022; Li et al., 2022; Liu et al., 2022; Zhang et al., 2022). Two main models are in dispute. The first is a hard collision caused by northward subduction (Han et al., 2020; Wang et al., 2020; Yan and Zhang, 2020) and the second is a soft collision caused by DDS (Zhu et al., 2016; Li S. M. et al., 2018; Li et al., 2019; Luo A. B. et al., 2022a; Luo A-B. et al., 2022b; Shi et al., 2022). The former is supported by the following: 1) A subduction complex (Mugagangri Formation) is distributed along the BNSZ and the southern Qiangtang Terrane (Hu W-L. et al., 2022). 2) continent-arc igneous rocks are distributed in the southern margin of the Qiangtang Terrane (Li S-M. et al., 2014; Tong et al., 2022). 3) The dip direction of thrust fault at the edge of the BNSZ is northward (Kapp et al., 2007). The latter is evidenced by the following points: 1) Early Cretaceous adakites and sodium-rich rocks occur in the northern margin of the Lhasa Terrane and the southern margin of the Qiangtang Terrane (Li X. K. et al., 2018; Liu et al., 2020). 2) High-resolution seismic reflection data reveals the Mesozoic DDS relict preserved within the crust. (Shi et al., 2022). 3) The comprehensive research on lava (High-K quartz-diorites, low-K tholeiitic andesites, bajaitic latites) in southern Qiangtang and sediments records the process from DDS to soft collision (Li et al., 2019).

To test the two disputed models, we selected bimodal volcanic rocks in the Wuga Co Lake for the following three reasons: 1) Felsic igneous rocks are easier to date than the mafic rocks; 2) The bimodal volcanic rocks are located in BNSZ, and such sample reports are scarce; and 3) Unveiling the petrogenesis of these samples has important implications for tracing the collisional orogenic processes between the northern Lhasa and southern Qiangtang terranes. Therefore, new geochemical and geochronological evidence for the bimodal volcanic rocks in the Wuga Co area is presented in this paper. These data, together with Hf isotopic data, allow us to investigate the evolution of the BNSZ.

2 Geological background and samples

The Tibetan-Himalayan Plateau is the highest plateau on Earth. It is a continuous accretion of the Songpan-Ganzi, Qiangtang, Lhasa, and Indian terranes. These terranes are separated by the Jinsha Suture Zone, Bangong–Nujiang Suture Zone, and Indus-Yarlung Zangbo Suture zones from north to south, respectively (Chang and Lo, 1973; Wang and Wright, 1987; Yin and Harrison, 2000) (Figures 1A, B). Furthermore, the Lhasa Terrane is subdivided into northern, central, and southern terranes by the Shiquan River-Nam Tso Mélange Zone and the Luobadui-Milashan Fault. The Qiangtang Terrane is subdivided into northern and southern parts by the Longmu Co-Shuanghu Mélange Zone.

The Cretaceous volcanic rocks in the north-central Lhasa Terrane include the Zenong Group and the Duoni Formation, as well as the Qushenla Formation in the southern part of the BNSZ (Zhu et al., 2016). The widespread Jurassic and Cretaceous magmatic activity in the north-central Lhasa Terrane is interpreted as the subduction of the BNO and continental collision (Li et al., 2015a; Hao et al., 2016a; Zhu et al., 2016; Yang and Wang, 2019). The Early Cretaceous Zenong Group contains high-K calc-alkaline felsic magma and pyroclastic rocks with an average thickness of 1000 m and an area of about 20000 km^2 (Chen et al., 2014). The eruption age of the Duoni Formation is 115–100 Ma, and the main lithology is basaltic andesite and rhyolite, with a thickness of 3000 m (Zhu et al., 2016). The Qushenla Formation is sparsely distributed and consists of andesite and minor basaltic andesite (Zhu et al., 2016).

Early studies in the sourthern Qiangtang Terrane found no evidences of arc magmatism. The lack of evidences for magmatic action in the BNSZ hinders its understanding (Allégre et al., 1984; Zhu et al., 2016). Later, identification of 185–170 Ma granitoids in the Amdo microplate, interpreted as a Jurassic continental arc along the sourthern Qiangtang Terrane, provides evidences of northward subduction (Guynn et al., 2006). Recent studies show that many Jurassic to early Cretaceous (181–101 Ma) arc-type igneous rocks are located within the southern Qiangtang Terrane. The lithology of these magmatic rocks consists of gabbroic diorites, diorites, granodiorites, and granites (Kapp et al., 2005; Li J-X. et al., 2014; Ran et al., 2015).

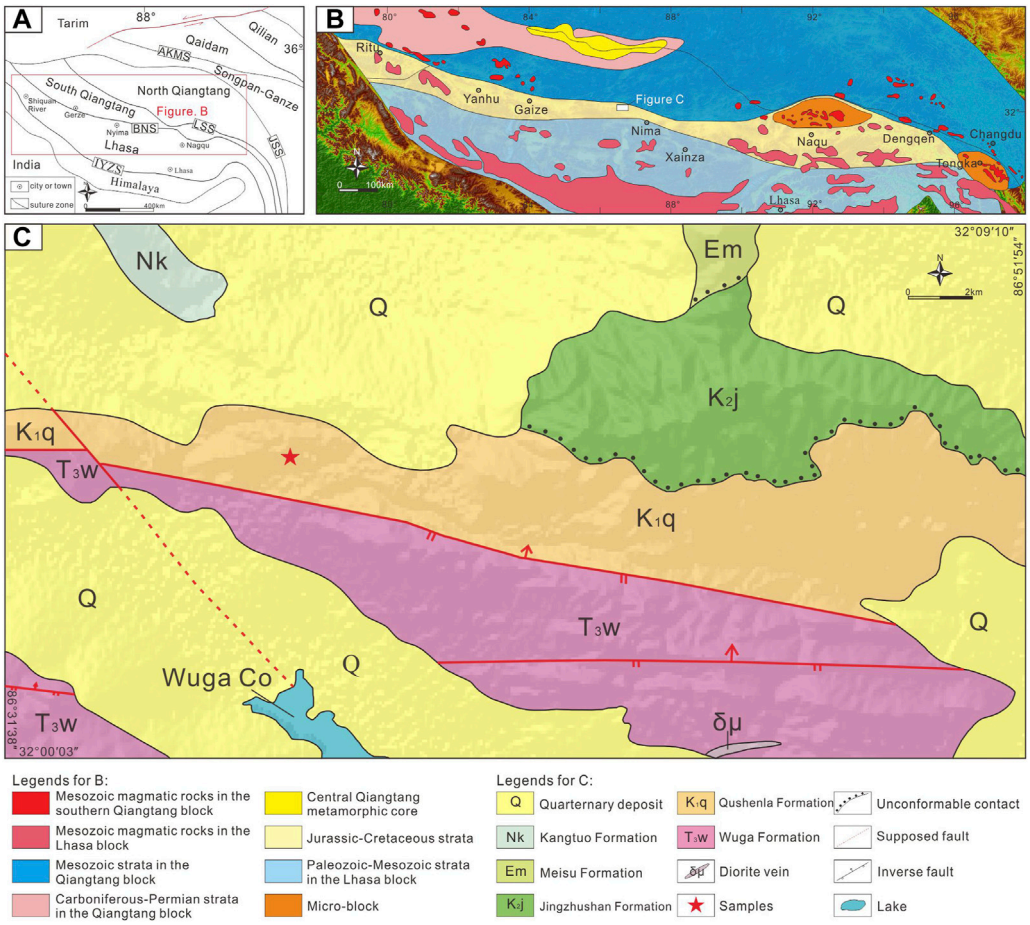

FIGURE 1
(A) Tectonic framework of the Himalaya-Tibetan Plateau; **(B)** Simplified geological map of central Tibet showing the spatial distribution of Mesozoic magmatic rocks along the Bangong-Nujiang Suture Zone (BNSZ) and the study area; **(C)** Geological map of the Wuga Co area, showing the locations of the samples. Abbreviations of tectonic terranes are as follows: IYZS, Indus-Yarlung Zangbo Suture Zone, BNS, Bangong-Nujiang Suture Zone; LSS, Longmu Co-Shuanghu Suture Zone; JSS, Jinshajiang Suture Zone; ANMS, Ayimaqin Suture Zone.

The BNSZ spans more than 2,000 km in central Tibet, and is characterized by flysch, mélange, and ophiolite fragments, representing remnants of the BNO (Zhu et al., 2016). In the BNSZ, the complete ophiolite sequence has been found in the areas of Ritu, Dongcuo, Dongqiao, Amdo, and Dingqing (Fan et al., 2014; Liu et al., 2014; Zhu et al., 2016). The Early Cretaceous Shamuluo Formation is unconformable on ophiolite rocks and flysch. The Jurassic Mugagangri Formation flysch consists of deformed deep-sea turbidites and ophiolite remnants. The lithology of the Shamuluo Formation is mainly sandstone and limestone deposited in a shallow marine environment (Zhu et al., 2016).

The Qushenla Formation rocks have Wuga Co basaltic andesites (WGBA) and Wuga Co rhyolites (WGR) sandwiched within WGBA and have an extent of approximately 530 km^2, located approximately 52 km northwest of Nima County in the Wuga Co area (Figures 1B, C). The Qushenla Formation unconformably contacts the Jingzhushan Formation and contacts the Late Triassic Wuga Formation along a fault (Figure 1C).

The basaltic andesite is gray black, massive, and porphyritic (Figures 2A, B). The basaltic andesite contains plagioclase phenocrysts and a microcrystalline matrix (Figure 2C). Plagioclase grains are euhedral and elongate and show polysynthetic twinning. These phenocrysts are about 0.5 mm long and 0.1 mm wide. Thin section observations indicate alteration. The occurrence of chlorite were altered from plagioclase and the carbonation were altered from matrix. The WGR is grayish brown and rhyotaxitic (Figure 2D). The phenocrysts are mainly quartz and have a preferred orientation. The length of quartz grains is 0.2–0.4 mm, and the width is about 0.05 mm. No alteration is found under microscope.

3 Analytical methods

3.1 Zircons U-Pb dating and Hf isotope analyses

U-Pb dating and trace element analysis of zircon were simultaneously conducted by laser ablation inductively coupled plasma mass spectrometry (LA-ICP-MS) at the Wuhan

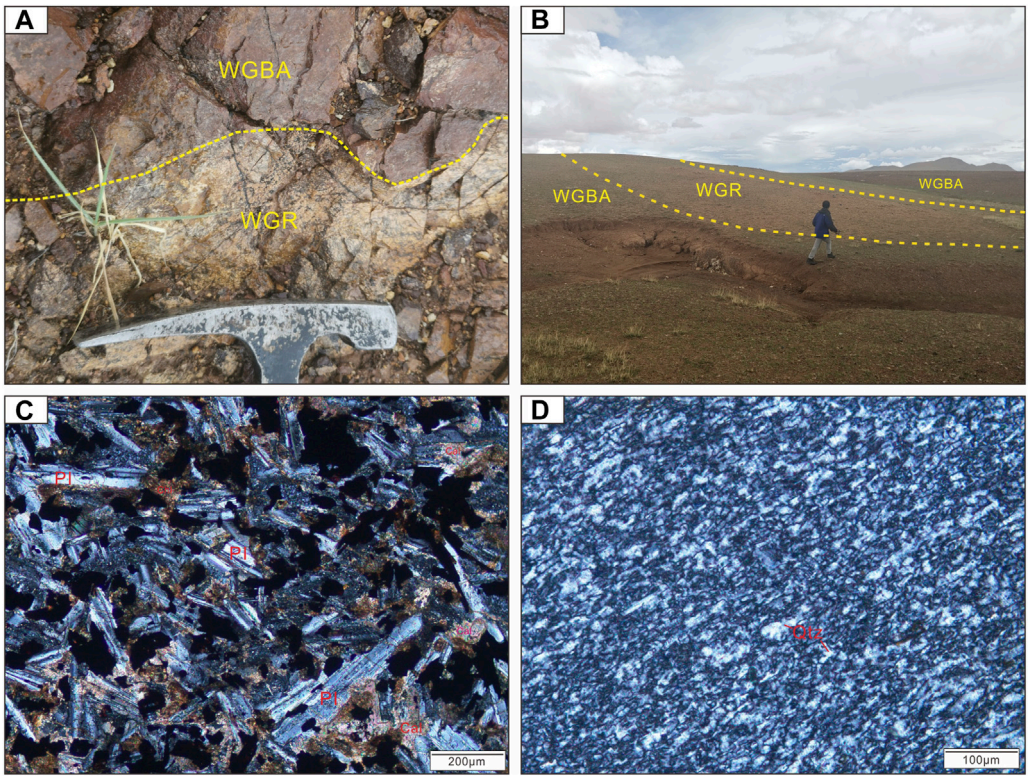

FIGURE 2
(A, B) Outcrop photographs showing field characters of representative bimodal rocks in the Wuga Co area; **(C)** Microphotographs showing textures and mineral assemblages of the Wuga Co basaltic andesites (WGBA); **(D)** Microphotographs showing textures and mineral assemblages of the Wuga Co rhyolites (WGR).

SampleSolution Analytical Technology Co., Ltd. (Wuhan, China). Detailed operating conditions for the laser ablation system, the ICP-MS instrument, and the data reduction are given in Zong et al. (2017). Laser sampling was performed using a GeolasPro laser ablation system that consists of a COMPexPro 102 ArF excimer laser (wavelength of 193 nm and maximum energy of 200 mJ) and a MicroLas optical system. An Agilent 7900 ICP-MS instrument was used to acquire ion-signal intensities. Helium was applied as a carrier gas. Argon was used as the make-up gas and mixed with the carrier gas *via* a T-connector before entering the ICP. A wire signal-smoothing device is included in this laser ablation system (Hu et al., 2015). The spot size and frequency of the laser were set to 30 μm and 6 Hz, respectively. Zircon 91500 and glass NIST610 were used as external standards for U-Pb dating and trace-element calibration, respectively. Each analysis incorporated a background acquisition of approximately 20–30 s followed by 50 s of data acquisition from the sample. An Excel-based software ICPMSDataCal was used to perform off-line selection and integration of the background and analyzed signals, time-drift correction, and quantitative calibration for trace-element analysis and U-Pb dating (Liu et al., 2008; Liu Y. et al., 2010). Concordia diagrams and weighted mean calculations were made using Isoplot/Ex_ver3 (Ludwig, 2003).

In situ zircon Hf isotope analyses were performed on 36 previously dated zircon grains from the WGR samples. The points used for the Hf analyses were the same as those used during the LA-ICP-MS analyses, which were selected from cathodoluminescence (CL) images. The data were collected using a NEPTUNE Plus MC-ICP-MS. A single spot ablation mode with a spot size of 55 μm was used to acquire the data. Each measurement consisted of 20 s of background signal acquisition followed by 50 s of ablation signal acquisition. Detailed information on the operating conditions and analytical methods can be found in Hu et al. (2012). The analyzed $^{176}Hf/^{177}Hf$ ratios for the zircon standard (91500) were 0.282299 ± 31 (2σ n, n = 40), which are similar to the $^{176}Hf/^{177}Hf$ ratios of 0.282302 ± 8 and 0.282306 ± 8 (2σ) for the standard when determined by the solution method (Goolaerts et al., 2004; Jon et al., 2004). Off-line selection, integration of analyte signals, and mass bias calibrations were performed using the ICPMSDataCal program (Liu Y. S. et al., 2010b).

3.2 Whole-rock Nd isotopic compositions

Nd isotope analyses were performed on a Neptune Plus MC-ICP-MS (Thermo Fisher Scientific, Dreieich, Germany) at the Wuhan SampleSolution Analytical Technology Co., Ltd. (Wuhan, China). The exponential law, which initially was developed for thermal ionization mass spectrometry measurement (Russell et al., 1978) and remains the most widely accepted and used with MC-ICP-MS, was used to assess the instrumental mass discrimination in this study. The

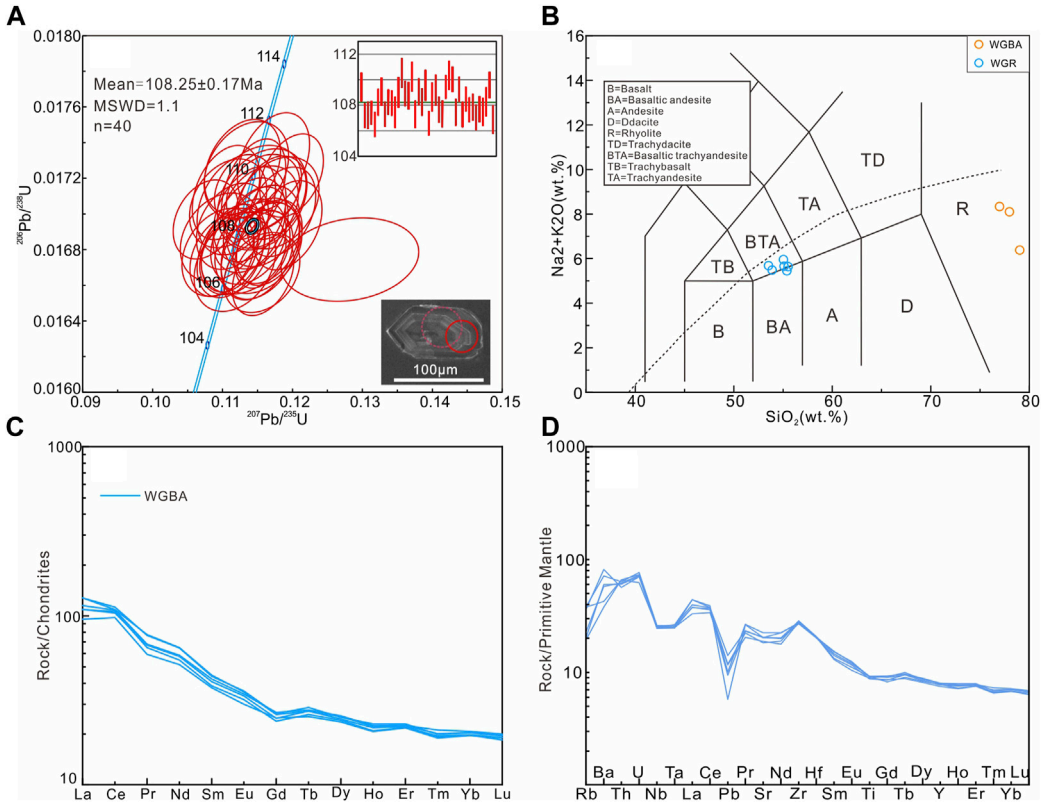

FIGURE 3
(A) Concordia plots of studied rocks in the Wuga Co area and Cathodoluminescence (CL) images of representative zircon grains. The solid and dashed circles indicate the locations of laser ablation inductively coupled plasma mass spectrometry (LA-ICP-MS) U-Pb dating and Hf analyses, respectively; **(B)** Total Alkali-Silica (TAS) diagram; **(C)** Chondrite-normalized rare-earth element (REE) patterns; **(D)** primitive-mantle-normalized trace element patterns for the Wuga Co basaltic andesites (WGBA).

remaining interferences of $^{144}Sm^{+}$ were corrected based on the method described by Jie et al. (2016). All data reduction for the MC-ICP-MS analysis of Nd isotope ratios was conducted using Iso-Compass software (Zhang et al., 2020). One GSB 04-3258–2015 standard was measured for every seven samples analyzed. Analyses of the standard yielded a $^{143}Nd/^{144}Nd$ ratio of 0.512440 ± 6 (2σ, n = 31), which is identical within error to published values 0.512438 ± 6 (2σ) (Jie et al., 2016). In addition, the USGS reference materials BCR-2 (basalt) and RGM-2 (rhyolite) yielded ratios of 0.512641 ± 11 (2σ, n = 82) and 0.512804 ± 12 (2σ, n = 80) for $^{143}Nd/^{144}Nd$, respectively, which are identical within error to published values (Li C-F. et al., 2012).

3.3 Whole-rock major and trace elements

Whole rock elements compositions of samples were analyzed at Wuhan SampleSolution Analytical Technology Co., Ltd., Wuhan, China. Major element abundances were determined using Zsx Primus II wavelength dispersive X-ray fluorescence spectrometer (XRF). The agate crushed sample was dried first at 106°C for 2–4 h. After it, 25 g of the annealed sample was mixed with 5 g of sodium tetraborate in platinum crucible. This mixture was melted in high frequency furnace. After cooling, the melt was diluted to 100 ml by adding water. All major element analysis lines are kα and the standard curve uses the national standard materials, rock standard sample: GBW07101-14 The data were corrected by theoretical α coefficient method. The relative standard deviation (RSD) is less than 2%.

Trace element analysis of whole rock were conducted on Agilent 7700e ICP-MS at the Institute of Mineral Resources, Chinese Academy of Geological Sciences. The detailed sample-digesting procedure was as follows: 1) Sample powder (200 mesh) were placed in an oven at 105°C for drying of 12 h; 2) 50 mg sample powder was accurately weighed and placed in a Teflon bomb; 3) 1 ml HNO_3 and 1 ml HF were slowly added into the Teflon bomb; 4) Teflon bomb was putted in a stainless steel pressure jacket and heated to 190°C in an oven for >24 h; 5) After cooling, the Teflon bomb was opened and placed on a hotplate at 140°C and evaporated to incipient dryness, and then 1 ml HNO_3 was added and evaporated to dryness again; 6) 1 ml of HNO_3, 1 ml of MQ water and 1 ml internal standard solution of 1ppm In were added, and the Teflon bomb was resealed and placed in the oven at 190°C for >12 h; 7) The final solution was transferred to a polyethylene bottle and diluted to 100 g by the addition of 2% HNO_3.

10.3389/feart.2023.1108655

TABLE 1 Major (wt%) and trace element (ppm) compositions.

Sample	nb-1	nb-2	nb-3	nb-6	nb-7	nb-9	nb-10	nb-12	nb-13
Lithology	WGR			WGBA					
SiO_2	79.05	77.98	76.99	55.52	55.05	53.90	55.11	55.39	53.53
TiO_2	0.21	0.23	0.24	1.98	1.97	1.96	1.97	2.03	2.07
Al_2O_3	11.92	12.92	13.31	18.11	17.87	17.41	17.84	17.90	18.32
TFe_2O_3	0.80	0.40	0.69	10.49	7.52	12.23	9.23	9.55	8.12
MnO	0.01	0.01	0.01	0.10	0.16	0.12	0.13	0.10	0.14
MgO	0.09	0.04	0.05	1.27	1.61	0.93	1.40	0.56	0.96
CaO	1.51	0.27	0.32	6.40	9.39	7.49	8.20	8.52	10.68
Na_2O	5.55	5.67	5.09	4.93	4.66	4.44	4.69	4.53	4.99
K_2O	0.83	2.43	3.24	0.70	1.28	1.04	0.95	0.91	0.68
P_2O_5	0.05	0.05	0.05	0.48	0.48	0.48	0.48	0.50	0.51
LOI	1.77	0.64	0.84	3.73	4.20	3.89	3.88	4.38	7.30
SUM	97.71	99.73	98.87	95.67	95.82	95.39	95.73	94.95	93.18
Li	4.83	8.58	7.96	11.19	14.22	3.54	18.58	13.68	23.98
Be	1.36	1.37	1.66	2.49	2.31	2.62	2.03	2.28	2.11
Sc	1.41	0.74	0.89	15.80	20.83	15.99	16.97	13.63	19.72
Ti	1241.72	1353.46	1430.70	11904.63	11921.67	11920.37	11281.13	11463.52	11682.21
V	11.47	8.39	14.90	208.40	209.37	212.85	195.98	200.72	198.98
Cr	5.01	6.11	9.13	43.91	44.71	39.71	36.83	39.63	42.08
Mn	85.56	53.37	68.44	788.37	1159.98	919.02	896.64	739.34	896.72
Co	1.43	1.32	1.77	21.23	27.36	19.17	21.98	21.47	16.27
Ni	2.91	3.08	3.06	23.98	28.40	22.72	23.96	23.98	18.91
Cu	16.01	7.29	5.27	18.23	18.50	17.01	22.55	19.04	27.00
Zn	10.19	6.50	13.50	89.30	81.30	91.50	75.60	63.00	81.10
Ga	13.67	9.58	11.69	23.12	23.42	23.01	22.77	21.51	23.02
Ge	1.75	2.01	1.96	1.86	1.71	2.24	1.73	1.76	1.52
As	29.27	29.99	49.39	16.82	5.71	38.44	11.68	24.95	9.92
Rb	22.69	40.63	55.88	14.41	24.00	24.15	12.84	22.87	12.30
Sr	140.63	39.76	43.44	383.17	471.26	427.30	430.68	396.65	427.52
Y	18.81	6.02	4.68	35.44	35.99	36.25	34.97	33.99	36.30
Zr	234.52	202.95	202.32	319.28	305.58	317.49	301.26	309.03	306.87
Nb	9.14	9.82	10.55	18.31	18.02	18.54	17.48	17.60	17.86
Mo	2.50	2.77	1.95	3.31	2.34	6.26	2.67	2.65	2.76
In	0.12	0.06	0.05	0.09	0.10	0.10	0.09	0.08	0.12
Cd	0.42	0.29	0.30	0.13	0.15	0.14	0.14	0.12	0.16
Sn	6.64	5.96	7.01	2.41	2.67	2.40	2.41	2.42	2.31
Sb	1.05	1.54	1.75	0.47	0.30	1.92	0.75	1.50	0.32
Cs	0.85	0.37	0.52	1.72	1.08	2.22	1.28	2.47	1.50

(Continued on following page)

TABLE 1 (*Continued*) **Major (wt%) and trace element (ppm) compositions.**

Sample	nb-1	nb-2	nb-3	nb-6	nb-7	nb-9	nb-10	nb-12	nb-13
Lithology	WGR			WGBA					
Ba	2655.00	187.15	235.43	402.14	296.98	499.32	419.01	570.86	264.40
La	23.38	9.45	11.16	25.79	30.25	27.22	25.84	22.60	30.24
Ce	34.16	14.66	18.40	64.93	66.53	66.15	63.50	59.76	68.93
Pr	4.39	1.63	1.68	6.16	7.34	6.46	6.38	5.61	7.28
Nd	14.63	5.60	5.69	25.55	30.29	27.29	26.87	23.97	30.12
Sm	2.95	1.07	0.98	5.89	6.81	6.47	6.23	5.74	6.71
Eu	0.32	0.10	0.10	1.85	2.05	1.99	1.94	1.74	2.08
Gd	2.37	0.80	0.74	4.88	5.35	5.50	5.07	5.11	5.41
Tb	0.47	0.17	0.14	0.97	1.02	1.04	1.02	0.95	1.07
Dy	2.96	1.01	0.85	6.11	6.43	6.49	6.20	5.97	6.37
Ho	0.61	0.20	0.17	1.18	1.25	1.27	1.23	1.17	1.30
Er	1.96	0.66	0.55	3.61	3.69	3.72	3.66	3.59	3.79
Tm	0.30	0.10	0.08	0.50	0.51	0.54	0.49	0.48	0.51
Yb	2.18	0.67	0.56	3.35	3.47	3.52	3.34	3.32	3.44
Lu	0.32	0.10	0.08	0.48	0.50	0.51	0.47	0.48	0.49
Hf	6.23	5.16	5.25	6.38	6.29	6.40	6.21	6.34	6.32
Ta	0.89	0.94	1.00	1.04	1.08	1.06	1.01	1.03	1.03
W	3.14	2.72	3.77	0.98	0.75	1.85	1.34	0.70	1.04
Tl	0.37	2.57	1.64	0.06	0.09	0.09	0.06	0.08	0.05
Pb	1.04	3.48	1.20	2.18	1.86	2.60	1.74	2.15	1.06
Bi	0.33	0.58	0.69	<0.05	0.19	<0.05	<0.05	0.08	0.11
Th	19.43	6.71	9.45	5.25	5.59	5.39	5.14	4.80	5.62
U	7.60	7.97	9.06	1.53	1.31	1.61	1.49	1.48	1.54
$Mg^{\#}$	18.15	16.50	13.56	19.29	29.73	13.07	23.09	10.39	19.04
$(La/Yb)_N$	7.70	10.08	14.21	5.51	6.26	5.56	5.56	4.88	6.30

4 Results

4.1 Zircon U-Pb ages

Forty zircon grains from rhyolite sample (nb-1) are euhedral, medium to long prismatic. The zircon grains have clear, linear oscillation zones (Figure 3A), indicating the magmatic origin. They are 50–150 μm in length, with aspect ratios ranging from 1:1 to 2:1. These zircons have relatively various U (287–1489 ppm) and uniform Th (557–1579ppm) contents, and high Th/U ratios (0.51–0.95), similar to magmatic zircons with Th/U>0.5 (Hoskin and Schaltegger, 2003). The zircon $^{206}Pb/^{238}U$ ages ranged from 106.5 ± 3.2 Ma to 110.5 ± 3.6 Ma with a weighted average of 108.25 ± 0.17 Ma (1σ; MSWD = 1.1; Figure 3A). The zircon U-Pb dating results are listed in Supplementary Table S1.

4.2 Major and trace element data

4.1.1 The WGBA

The WGBA samples (SiO_2 = 53.5–55.5 wt%) have low MgO (0.56–1.61 wt%), $Mg^{\#}$ (10.4–29.7), Cr (37–45 ppm), and Ni (19–8 ppm). These samples are characterized by high Ti (1.1–1.2 wt%), Al_2O_3 (17.4–18.3 wt%), and P_2O_5 (0.48–0.51 wt%) contents. In the total alkali vs. silica (TAS) classification diagram (Figure 3B), the samples plot predominantly within the sub-alkaline and basaltic andesite fields. They are slightly enriched in LREEs [$(La/Yb)_N$ = 4.88–6.30] and depleted in high field strength elements (HFSEs; e.g., Nb = 17.5–18.5 ppm and Zr = 301–319 ppm) with weakly negative Nb-Ta-Ti anomalies in the primitive mantle-normalized variation diagrams (Figures 3C, D). The major and trace whole-rock data are presented in Table 1.

TABLE 2 Whole-rock Sr–Nd isotopic compositions.

Sample	Rb	Sr	$^{87}Sr/^{86}Sr$		$(^{87}Sr/^{86}Sr)i$	Sm	Nd	$^{143}Nd/^{144}Nd$		εNd(0)	$(^{143}Nd/^{144}Nd)T$	εNd(t)	f Sm/Nd
	ppm	ppm	ratio	2σ		ppm	ppm	ratio	2σ				
nb-1	22.69	140.63	0.707079	0.000005	0.706362	2.95	14.63	0.512709	0.000004	1.38	0.512623	2.42	−0.379880
nb-2	40.63	39.76	0.707922	0.000006	0.703381	1.07	5.60	0.512696	0.000003	1.13	0.512614	2.25	−0.411665
nb-3	55.88	43.44	0.708737	0.000008	0.703021	0.98	5.69	0.512700	0.000003	1.21	0.512626	2.49	−0.470718
nb-6	14.41	383.17	0.704309	0.000007	0.704142	5.89	25.55	0.512806	0.000004	3.28	0.512708	4.07	−0.291385
nb-9	24.15	427.30	0.704244	0.000006	0.703993	6.47	27.29	0.512797	0.000004	3.10	0.512696	3.84	−0.270845
nb-12	22.87	396.65	0.70442	0.000007	0.704164	5.74	23.97	0.512798	0.000004	3.12	0.512696	3.84	−0.263875
nb-13	12.30	427.52	0.704494	0.000006	0.704366	6.71	30.12	0.512800	0.000003	3.16	0.512705	4.02	−0.315081

4.1.2 The WGR

The WGR samples have high aluminum (Al_2O_3 = 11.9–13.3wt %), variable K_2O (0.83–3.24 wt%), low TiO_2 (0.21–0.24 wt%), and low MgO (0.04–0.09 wt%) contents. They are characterized by high silicon (SiO_2 = 76.99–79.05 wt%) and low total alkali contents (Na_2O+K_2O = 6.38–8.33 wt%), plotting in the subalkaline-rhyolite fields in the TAS diagram (Figure 3B). Furthermore, They have relatively high La, low Yb and high $(La/Yb)_N$, indicating obvious fractionation between light rare-earth elements (LREEs) and heavy rare-earth elements (HREEs). The major and trace-element whole-rock data are presented in Table 1.

4.3 *In situ* zircon Lu-Hf isotopes

Thirty-nine Hf isotopic analyses were carried out on 39 zircons separated from the WGR (nb-1). The initial $^{176}Hf/^{177}Hf$ ratios of the WGR samples vary from 0.282864 to 0.282987. The zircon εHf(t) values range from +5.6 to +10.0 and hafnium model ages range from 368.4 Ma to 539.9 Ma. The zircon Lu-Hf isotope data are listed in Supplementary Table S2.

4.4 Whole-rock Sr-Nd isotopes

The WGBA samples have low initial $^{87}Sr/^{86}Sr$ ratios (0.703993–0.704366) and high initial $^{143}Nd/^{144}Nd$ ratios (0.512695–0.512708). εNd(t) values vary from +3.8 to +4.1. The WGR samples have variable initial $^{87}Sr/^{86}Sr$ ratios (0.703381–0.706362) and high initial $^{143}Nd/^{144}Nd$ ratios (0.512614–0.512626). εNd(t) values vary from +2.2 to +2.5. The whole-rock Sr-Nd isotopic composition data are presented in Table 2.

5 Discussion

5.1 Petrogenesis process

5.1.1 The WGBA

The petrogenesis of basaltic andesite is complex and several hypotheses have been proposed (Kuno, 1968; Boettcher, 1973; Grove and Kinzler, 1986; Grove et al., 2002). In general, the basaltic andesite genesis process can be summarized into three types: 1) Fractional crystallization (FC) in a shallow crustal magma chamber following partial melting of basaltic magma from the mantle (Sisson and Grove, 1993; Grove et al., 1997). 2) Mixing of basaltic magma from the mantle with felsic magma from the crust (Heiken and Eichelberger, 1980). 3) Partial melting of mantle wedge peridotite that interacts with subducted oceanic crustal melt, or fluids and/or melts from subducted sediments. (Tatsumi, 1982; Parman and Grove, 2004).

Significant FC for these basaltic andesites can be ruled out, for the following four reasons: 1) An obvious linear relationship is not shown in the Harker diagram (Supplementary Figure S1). 2) Basaltic andesites produced by FC require basaltic magma as the parent magma; however, no contemporaneous basaltic magma has emerged around the study area (Zheng et al., 2015). 3) The FC of plagioclase is often accompanied with negative Eu anomalies, which is not shown in our samples (Figure 3C). 4) The WGBA samples show no FC trend in the La/Sm *versus* La diagrams or La/Yb *versus* La diagrams (Figures 4A, B).

The mixture of mafic magma and felsic magma can produce basaltic andesite magma. However, the signature of homogeneous isotopic values ($^{87}Sr/^{86}Sr$ = 0.704244–0.704494, $^{143}Nd/^{144}Nd$ = 0.512797–0.512806) suggests that no magma mixing occurred (Yang et al., 2012). Moreover, neither enclaves nor disequilibrium textures were observed in the field or microscope observations (Figure 2C; Perugini and Poli, 2012; Liu et al., 2019). Further support for this conclusion is given by the consistent chondrite-normalized REE and primitive-mantle-normalized trace-element patterns (Figures 3C, D; Liu et al., 2019).

In the process of partial melting and fractional crystallization, the distribution coefficient of strongly incompatible elements relative to compatible elements can be ignored. According to this, Allègre and Minster, (1978) has carried out graphical and theoretical derivation for partial melting and fractional crystallization. When the concentration ratio of strongly incompatible elements to compatible elements is plotted against the concentration of strongly incompatible elements, the trajectory of partial melting is an inclined line, while the separation crystallization is a horizontal line. The values of WGBA have a strong positive correlation in the La/Yb *versus* La diagrams and that

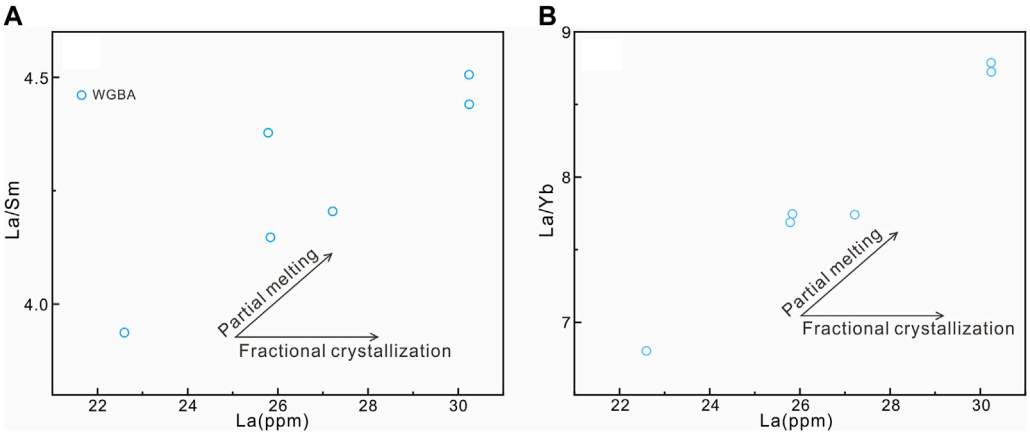

FIGURE 4
(A) La/Sm *versus* La diagrams for the Wuga Co basaltic andesites (WGBA); **(B)** La/Yb *versus* La diagrams for the WGBA. Data and symbols are the same as in Figure 3B.

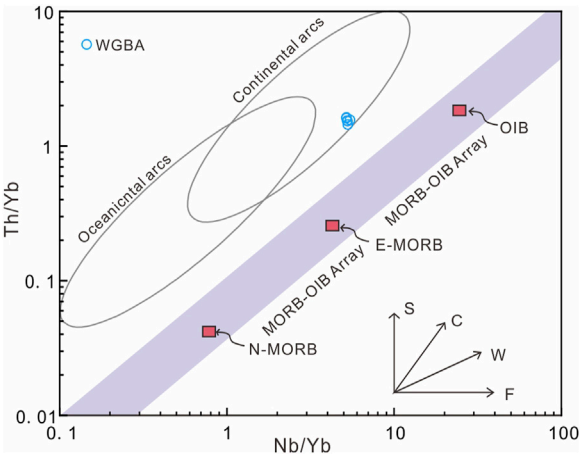

FIGURE 5
Nb/Yb vs. Th/Yb diagram (Pearce, 2008) of the Wuga Co basaltic andesites (WGBA) from the Wuga Co area. S, C, W, and F refer to enrichment by subduction environment, continental contamination, enrichment within plate, and fractional crystallization, respectively. Data and symbols are the same as in Figure 3B.

in the La/Sm *versus* La diagrams (Figures 4A, B), which is consistent with partial melting trends. Therefore, we suggest that the WGBA samples were generated by partial melting of their source rocks. Therefore, their source characteristics can be represented by their geochemical features.

5.1.2 The WGR

The WGBA (SiO_2 = 53.9–55.5wt%) interbedded with the WGR (SiO_2 = 77.0%–79.0wt%) constitute a bimodal volcanic suite. Two models have been proposed to explain the siliceous composition of bimodal volcanic rocks (Sui and Wang, 2013): 1) Crustal anatexis induced by the heat energy from the basaltic magma with distinct isotopic composition (Roberts and Clemens, 1993; Tepper et al., 1993; Guffanti et al., 1996; Zhu et al., 2007; Zhu et al., 2012); or, 2) FC of mantle-derived magma with similar isotopic compositions (Bacon and Druitt, 1988; Pin and Paquette, 1997; Bonin, 2004).

Partial melting and fractional crystallization cannot change the isotope ratios. The distinct differences of the εNd(t) values between the WGBA (+3.8 to +4.0) and the WGR (+2.2 to +2.5) rule out the FC model. Furthermore, FC trends of the WGR were not observed in the Harker diagram (Supplementary Figure S1) and the low $Mg^{\#}$ values (13.5–18.2) of the WGR are consistent with crustal melts ($Mg^{\#}$<40) (Rapp and Bruce Watson, 1995; Wei et al., 2017). All these geochemical characteristics suggest that the WGR resulted from crustal anatexis.

5.2 Magma source

5.2.1 The WGBA

We suggest that the WGBA are derived from mantle peridotite because they have low $^{87}Sr/^{86}Sr$ values (0.703993–0.704366) and high ε(Nd) values (3.84–4.07). Nb, Ta, and Hf elements have the same geochemical behavior because of their similar incompatibility during magmatic evolution. The values of Nb/Ta and Hf/Ta can reflect the features of the source, because they do not change during partial melting or FC (Pearce and Peate, 1995; Wang et al., 2021; Zhao et al., 2021). The Nb/Ta (16.67–17.62) and Hf/Ta (5.82–6.18) values of our samples are similar to those of the primitive mantle (Nb/Ta = 17.39, Hf/Ta = 7.54), providing further evidences for their derivation from mantle peridotite. However, in the Th/Yb *versus* Nb/Yb diagram, the WGBA samples are distributed above the MORB-OIB array (Figure 5). Therefore, we suggest that there are other endmembers involved in the source region of the WGBA (Pearce, 2008; Huang et al., 2017; Wei et al., 2017; Xu et al., 2017; Zhong et al., 2017; Tang et al., 2018).

In the Ni *versus* Cr diagram, the WGBA samples plot on the mixing line between slab melt and mantle peridotite (Figure 6A), similar to the Biluoco magnesian andesite which is derived from the interaction between mantle peridotite and slab-derived materials

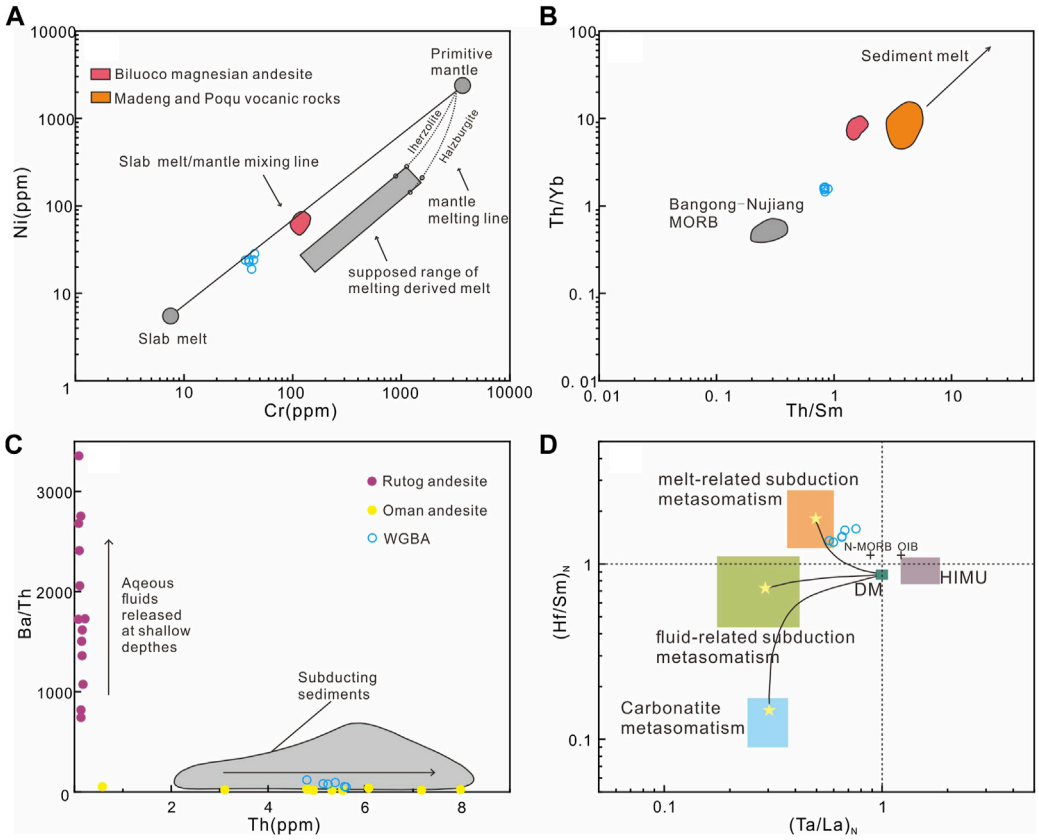

FIGURE 6
(A) Ni-Cr plots for the Wuga Co basaltic andesites (WGBA; Tsuchiya et al., 2005); **(B)** Th/Yb *versus* Th/Sm for the WGBA. Literature data about the Biluoco magnesian andesite and Madeng and Poqu volcanic rocks are from He et al. (2018) and references therein. **(C)** Ba/Th *versus* Th diagram (Perez et al., 2018); **(D)** $(Hf/Sm)_N$ *versus* $(Ta/La)_N$ diagram (La Flèche et al., 1998). Literature data about the Rutog andesite and Oman andesite are from Zhao et al. (2021) and Kanayama et al. (2012), respectively. Related data about subducting sediments is from Zhao et al. (2020). Data and symbols are the same as in Figure 3B.

(He et al., 2018). In addition, The WGBA also show the characteristics of low Y and heavy rare Earth elements (HREE; Figure 3C), which are generated by garnet residue in the source. These features, combined with high Na_2O/K_2O values (3.6–7.0), can be interpreted as the involvement of oceanic crust in the source region of the WGBA (He et al., 2018). In summary, the oceanic slab is part of the WGBA source materials.

The WGBA samples show not only the geochemical characteristics of oceanic slab but also the geochemical characteristics of sedimentary rocks. The ratios of Th/Yb in volcanic rocks can be used to identify the involvement of sediments and/or sediment-derived melts in their generation (Woodhead et al., 2001). On plots of Th/Yb *versus* Th/Sm (Figure 6B), the WGBA samples lie on the array between MORB and marine sediments, which indicates an obvious contribution from sediments in their origin (Li et al., 2015a). The sedimentary rock characteristics are also shown by the Ba/Th *versus* Th diagram (Figure 6C).

Furthermore, we suggest that the endmember of the sediments in the WGBA source area is likely from the accretionary wedge because of the enrichment in large-ion lithophile elements (LILE) and depletion in HFSE (Figure 3D). Previous studies have shown that there are three reasons for LILE enrichment and HFSE depletion: 1) Crustal contamination (Sun and McDonough, 1989; Li et al., 2017); 2) Involvement of aqueous fluids under a continental arc (Hawkesworth et al., 1993; Pearce and Parkinson, 1993; Li Y. J. et al., 2012; Chai et al., 2015); and 3) Involvement of mélange rocks (Marschall and Schumacher, 2012; Hao et al., 2016b). It has been explained in 5.1.1 that crustal contamination did not occur during petrogenesis. The involvement of aqueous fluids has been excluded by the Ba/Th *versus* Th diagram (Figure 6C) and $(Hf/Sm)_{PM}$ *versus* $(Ta/La)_{PM}$ diagram (Figure 6D) because the WGBA samples lie out the trend of aqueous fluids. Therefore, the conclusion that the mélange participates in the source rocks of the WGBA can be supported by the geochemical features of HFSE depletion and LILE enrichment. All these geochemical features indicate that sedimentary rocks in the accretionary wedge are involved in the source.

In summary, the geochemical data suggest that the WGBA is likely derived from partial melting of a mantle peridotite that interacted with subducted slab melts and melts from sediments in the accretionary wedge.

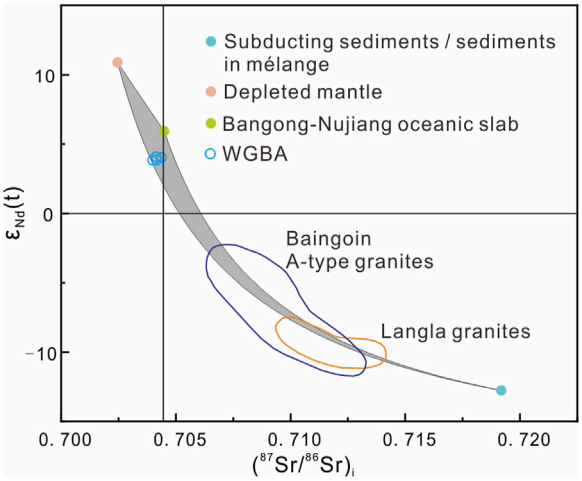

FIGURE 7
Plots of $(^{87}Sr/^{86}Sr)_i$ *versus* εNd(t). Related data about the Baingoin A-type granites and Langla granites are from Hu et al. (2019) and references therein. The values for subducting sediments in the Bangong-Nujiang Suture Zone (BNSZ), depleted mantle, and Banggong-Nujiang oceanic slab are from (Li J-X. et al., 2016; Rehkamper and Hofmann, 1997; Wang et al., 2016), respectively. The εNd(t) and $(^{87}Sr/^{86}Sr)_i$ values of these data have been modified to 108 Ma. Data and symbols are the same as in Figure 3B.

5.2.2 The WGR

The zircon in which Hf isotopes have a high closure temperature has a very low $^{176}Lu/^{177}Hf$ ratio. There is no significant radiogenic Hf accumulation after formation (Wu et al., 2007). Therefore, the $^{176}Hf/^{177}Hf$ ratio in zircon can represent the source characteristics. The zircons in the WGR have high ε(Hf) values (+5.6 to +10.0) and young two-stage model Hf ages (TDM2) values (516.6 Ma to 788.0 Ma), implying that they are derived from a juvenile basaltic crust.

In summary, the major and trace element geochemistry, together with the Nd-Hf isotopic compositions, suggest that the WGR is the product of partial melting of juvenile basaltic crust.

5.3 Isotopic evidences

To test that the source of WGBA is involved in the BNO sediments in accretionary wedge, depleted mantle and the BNO slab, it is necessary to determine the geochemical characteristics of the three endmembers.

A mélange is a disordered rock mixture formed by a combination of sedimentary rocks scraped from a subducted oceanic plate, some oceanic crust fragments, continental fragments, *in situ* sediments, and turbidite (Li C. et al., 2020). In this definition, the geochemical features of sediments in accretionary complex can be represented by the geochemical features of subducting sediments. In existing research, the assumed subducting sediments in the BNSZ, as represented by the Yanshiping Group sandstone from Duobuza (Figure 7), can be interpreted as sediments in accretionary complex (Li S-M. et al., 2016; Li J-X. et al., 2016).

The ophiolite has been interpreted as the remnants of the oceanic slab. The geochemical characteristics of ophiolite in BNSZ reported by previous studies can represent BNO slab (Wang, et al., 2016). On the other hand, the characteristics of depleted mantle under BNSZ have not been reported, so we quoted the global depleted mantle values (Figure 7).

The isotopic characteristics of WGBA that plotted among the BNO sediments in accretionary wedge, depleted mantle and the BNO slab (Figure 7) support that the WGBA samples are derived from partial melting of a mantle peridotite that interacted with subducted slab melts and melts from sediments in the accretionary wedge.

5.4 Geodynamic mechanism

5.4.1 Divergent double subduction and oceanic crust rupture

There are two main viewpoints in dispute about the subduction polarity of the BNO. Some studies have shown that the BNO subducted northward under the southern Qiangtang Terrane, and others support the conclusion that the BNO subducted not only northward beneath the southern Qiangtang Terrane but also southward beneath the northern Lhasa Terrane (Li D. et al., 2020; Ma et al., 2020; Peng et al., 2020; Jiang et al., 2021). Recent studies have shown that arc-related magmatic rocks are found on both sides of the BNSZ (Zhu et al., 2016). We consider that the BNO underwent DDS beneath the southern Qiangtang and the northern Lhasa terranes.

Because crust-mantle interaction is inevitable during mantle melting, the positive εHf(t) for the magmatic rocks in the Lhasa Terrane is likely underestimated, and should be higher (Zhu, 2011; Li Y. J. et al., 2020; Cao et al., 2022). Hence, the maximum value of εHf(t) collected is used as the participation degree of the mantle, which is reasonable. In a classical DDS system, the rupture from the overlying crust occurs at the initial stage of oceanic crust detachment. At this stage, mantle materials will fill the gap caused by the rupture, which would lead to the more mantle participate in the source of related magmatic rocks (Soesoo et al., 1997; Zhao, 2015; Zhu et al., 2016; Zhang et al., 2017). The maximum of collected ε(Hf) values in both the southern Qiangtang Terrane and the northern-central Lhasa Terrane increase at 130 Ma (Figure 8), simultaneously. Therefore, we suggest that the rupture of the BNO from both sides occurs at 130 Ma. This age has been endorsed by other studies (Zhu et al., 2016; Li Y. et al., 2018; Li et al., 2019).

5.4.2 Oceanic lithosphere sunk into the mantle

Soesoo et al. (1997) proposed that the magmatism caused by oceanic lithosphere completely sinking into the mantle has two characteristics. First, the related magmatic rocks are the products of three endmembers: sinking oceanic crust, mantle peridotite, and accretionary wedge sediments. Second, the related bimodal volcanic rocks are distributed in a hinge zone. The source of our sample similarly has three components: the BNO sediments in accretionary wedge, depleted mantle and the BNO slab (detailed explanation has

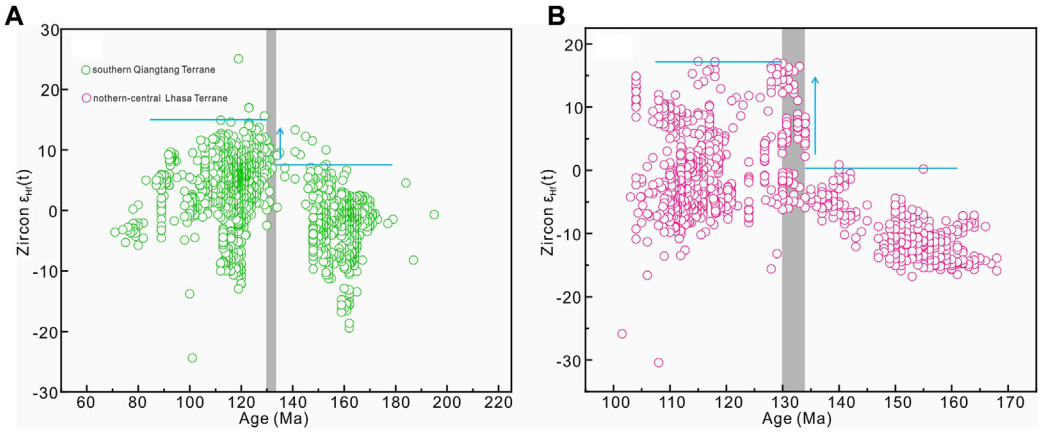

FIGURE 8
Zircon ages (Ma) *versus* εHf(t) values of igneous rocks from **(A)** southern Qiangtang Terrane and **(B)** northern-central Lhasa Terrane. Literature data are from Peng et al. (2020) and references therein, Cao et al. (2016) and references therein, Chen et al. (2017), and Yang et al. (2021). The summary of zircon Lu-Hf isotopic data is listed in Supplementary Table S3.

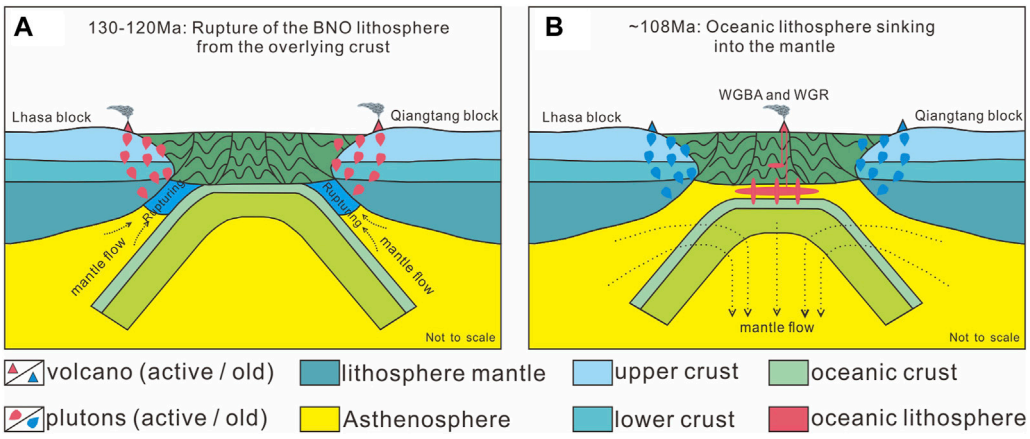

FIGURE 9
Evolution model for the terminal stage of divergent double-sided subduction in the Bangong-Nujiang Ocean. **(A)** Initial detachment of Bangong-Nujiang lithosphere; **(B)** sinking of Bangong-Nujiang oceanic slab.

been given in Section 5.2.1). In addition, the WGBA (SiO_2 = 53.9–55.5wt%) and interbedded WGR (SiO_2 = 77.0%–79.0wt%) constitute a bimodal volcanic suite. In summary, our sample is the product of the BNO slab sinking into the mantle, which occurred at approximately 108 Ma.

5.4.3 Geodynamic model

The sustained DDS eventually leads to the closure of the BNO (Zhu et al., 2016). The inverted U-shaped oceanic plate locked the flow of the asthenosphere. Therefore, magmatism was weak during this period (Zhu et al., 2016; Soesoo et al., 1997). However, closure of the oceanic basin leads to a locked but unstable situation. The continued sinking of the cold and dense BNO slab eventually led to its rupture from the two overlying terranes (southern Qiangtang and northern Lhasa terranes) at approximately 130 Ma (Figure 9).

Subsequently, the rupture propagates from both sides to the hinge zone, resulting in the BNO slab sinking into the mantle at 108 Ma. Mantle materials fill the gap between the sinking BNO slab and the BNSZ mélange, which results in the interaction of mantle peridotite, BNO slab, and accretionary wedge sedimentary rocks. The interaction led to the generation of the WGBA. The partial melting of oceanic crust fragments in hybrid rocks resulted in the generation of the WGR, which was attributed to continuous heating by the mantle flow.

The "slab sinking modal" in DDS have been first elaborated by Soesoo et al. (1997) to explain the Lachlan Belt in eastern Australia. This model has been applied in many other orogenic belts, such as the Precambrian Jiangnan Orogen in South China (Zhao, 2015), the Late Paleozoic-Mesozoic Xing'an-Mongolia Suture Zone in the Central Asian Orogenic Belt (Li S. M. et al., 2018; Pei et al., 2018). We take WGBA as an example to verify the rationality of

the "slab sinking model" in BNSZ. Furthermore, we make the first identification of direct products derived from slab sinking in the Bangong-Nujiang Suture Zone.

6 Conclusion

(1) In the Wuga Co area, the bimodal volcanic rocks of the Qushenla Formation are distributed within the BNSZ and were active at approximately 108 Ma. Sr-Nd isotope data of the samples plot among sedimentary rocks in mélange, mantle peridotite, and the BNO slab, which suggests that WGBA is the direct product of slab sinking.
(2) Hf isotope values of magmatic rocks on both sides of the BNSZ increased simultaneously at approximately 130 Ma, indicating the timing of the BNO slab rupture.
(3) BNO slab rupture from the two overlying terranes (southern Qiangtang Terrane and northern Lhasa Terrane) at approximately 130 Ma. With the rupture developing from both sides to the central BNSZ, the slab completely sank into the mantle at −108 Ma.

Data availability statement

The original contributions presented in the study are included in the article/Supplementary Material, further inquiries can be directed to the corresponding authors.

Author contributions

WC: Investigation and writing; ZL: Investigation and editing and polishing; NW: Investigation and editing GW: Editing and polishing; MZ: Investigation; NH: English polishing; YH: English polishing; XY: Investigation.

Funding

Geological survey of mineral resources in key prospective areas of strategic mineral resources (DD20221684).

Acknowledgments

We are deeply grateful to the reviewers for their constructive comments that improved the manuscript greatly. We thank editor for his efficient handling on this manuscript

Conflict of interest

Author MZ was employed by QingHai Salt Lake Industry Co, Ltd.

The remaining authors declare that the research was conducted in the absence of any commercial or financial relationships that could be construed as a potential conflict of interest.

Publisher's note

Supplementary material

The Supplementary Material for this article can be found online at: https://www.frontiersin.org/articles/10.3389/feart.2023.1108655/full#supplementary-material

References

Allégre, C. J., Courtillot, V., Tapponnier, P., Hirn, A., Mattauer, M., Coulon, C., et al. (1984). Structure and evolution of the Himalaya–Tibet orogenic belt. *Nature* 307 (5946), 17–22. doi:10.1038/307017a0

Allègre, C. J., and Minster, J. F. (1978). Quantitative models of trace element behavior in magmatic processes. *Earth Planet. Sci. Lett.* 38 (1), 1–25. doi:10.1016/0012-821X(78)90123-1

Bacon, C. R., and Druitt, T. H. (1988). Compositional evolution of the zoned calcalkaline magma chamber of Mount Mazama, Crater Lake, Oregon. *Contributions Mineralogy Petrology* 98 (2), 224–256. doi:10.1007/BF00402114

Boettcher, A. L. (1973). Volcanism and orogenic belts — the origin of andesites. *Tectonophysics* 17 (3), 223–240. doi:10.1016/0040-1951(73)90004-8

Bonin, B. (2004). Do coeval mafic and felsic magmas in post-collisional to within-plate regimes necessarily imply two contrasting, mantle and crustal, sources? A review. *LITHOS* 78 (1-2), 1–24. doi:10.1016/j.lithos.2004.04.042

Cao, H-W., Pei, Q-M., Santosh, M., Li, G-M., Zhang, L-K., Zhang, X-F., et al. (2022). Himalayan leucogranites: A review of geochemical and isotopic characteristics, timing of formation, Genesis, and rare metal mineralization. *Earth-Science Rev.* 234, 104229. doi:10.1016/j.earscirev.2022.104229

Cao, M. J., Qin, K. Z., Li, G. M., Li, J. X., Zhao, J. X., Evans, N. J., et al. (2016). Tectono-magmatic evolution of late jurassic to early cretaceous granitoids in the west central Lhasa subterrane, tibet. *Gondwana Res.* 39, 386–400. doi:10.1016/j.gr.2016.01.006

Chai, P., Sun, J-G., Xing, S-W., Men, L-J., and Han, J-L. (2015). Early cretaceous arc magmatism and high-sulphidation epithermal porphyry Cu–Au mineralization in yanbian area, northeast China: The duhuangling example. *Int. Geol. Rev.* 57 (9-10), 1267–1293. doi:10.1080/00206814.2014.960013

Chang, S., and Lo, D. (1973). An experimental system for the recognition of handwritten Chinese characters. *Proc. 1st Int. Symposium Comput. Chin. Input/Output Syst.*, 257–267.

Chen, S-S., Shi, R-D., Gong, X-H., Liu, D-L., Huang, Q-S., Yi, G-D., et al. (2017). A syn-collisional model for Early Cretaceous magmatism in the northern and central Lhasa subterranes. *Gondwana Res.* 41, 93–109. doi:10.1016/j.gr.2015.04.008

Chen, Y., Zhu, D-C., Zhao, Z-D., Meng, F-Y., Wang, Q., Santosh, M., et al. (2014). Slab breakoff triggered ca. 113Ma magmatism around Xainza area of the Lhasa Terrane, Tibet. *Gondwana Res.* 26 (2), 449–463. doi:10.1016/j.gr.2013.06.005

Fan, J. J., Li, C., Xie, C. M., and Wang, M. (2014). Petrology, geochemistry, and geochronology of the zhonggang ocean island, northern tibet: Implications for the evolution of the banggongco-nujiang oceanic arm of the neo-tethys. *Int. Geol. Rev.* 56 (12), 1504–1520. doi:10.1080/00206814.2014.947639

Girardeau, J., Marcoux, J., Allègre, C. J., Bassoullet, J. P., Tang, Y., Xiao, X., et al. (1984). Tectonic environment and geodynamic significance of the neo-cimmerian donqiao ophiolite, bangong-nujiang suture zone, tibet. *Nature* 307 (5946), 27–31. doi:10.1038/307027a0

Goolaerts, A., Mattielli, N., Jong, J. D., Weis, D., and Scoates, J. S. (2004). Hf and Lu isotopic reference values for the zircon standard 91500 by MC-ICP-MS. *Chem. Geol.* 206 (1-2), 1–9. doi:10.1016/j.chemgeo.2004.01.008

Grove, T. L., Donnelly-Nolan, J. M., and Housh, T. (1997). Magmatic processes that generated the rhyolite of glass mountain, medicine lake volcano, N. California. *Contributions Mineralogy Petrology* 127 (3), 205–223. doi:10.1007/s004100050276

Grove, T. L., and Kinzler, R. J. (1986). Petrogenesis of andesites. *Annu. Rev. Earth Planet. Sci.* 14, 417–454. doi:10.1146/annurev.ea.14.050186.002221

Grove, T., Parman, S., Bowring, S., Price, R., and Baker, M. (2002). The role of an H2O-rich fluid component in the generation of primitive basaltic andesites and andesites from the Mt. Shasta region, N California. *Contributions Mineralogy Petrology* 142 (4), 375–396. doi:10.1007/s004100100299

Guffanti, M., Clynne, M. A., and Muffler, L. P. J. (1996). Thermal and mass implications of magmatic evolution in the Lassen volcanic region, California, and minimum constraints on basalt influx to the lower crust. *J. Geophys. Research-Solid Earth* 101 (B2), 3003–3013. doi:10.1029/95JB03463

Guo, X., Li, C., Gao, R., Li, S., Xu, X., Lu, Z., et al. (2022). The India-Eurasia convergence system: Late Oligocene to early Miocene passive roof thrusting driven by deep-rooted duplex stacking. *Geosystems Geoenvironment* 1 (1), 100006. doi:10.1016/j.geogeo.2021.09.005

Guynn, J. H., Kapp, P., Pullen, A., Heizler, M., Gehrels, G., and Ding, L. (2006). Tibetan basement rocks near Amdo reveal "missing" mesozoic tectonism along the Bangong suture, central Tibet. *Geology* 34 (6), 505–508. doi:10.1130/G22453.1

Han, S., Li, H., Pan, J., Lu, H., Zheng, Y., Liu, D., et al. (2020). Genesis and geodynamic process of early Cretaceous intermediate–felsic batholith within the Chem Co zone, Western Qiangtang and implications for Bangong–Nujiang Tethyan Ocean subduction. *Gondwana Res.* 82, 193–220. doi:10.1016/j.gr.2019.11.017

Hao, L-L., Wang, Q., Wyman, D. A., Ou, Q., Dan, W., Jiang, Z-Q., et al. (2016a). Underplating of basaltic magmas and crustal growth in a continental arc: Evidence from Late Mesozoic intermediate–felsic intrusive rocks in southern Qiangtang, central Tibet. *Lithos* 245, 223–242. doi:10.1016/j.lithos.2015.09.015

Hao, L-L., Wang, Q., Wyman, D. A., Ou, Q., Dan, W., Jiang, Z-Q., et al. (2016b). Andesitic crustal growth via mélange partial melting: Evidence from Early Cretaceous arc dioritic/andesitic rocks in southern Qiangtang, central Tibet. *Geochem. Geophys. Geosystems* 17 (5), 1641–1659. doi:10.1002/2016gc006248

Hawkesworth, C. J., Gallagher, K., Hergt, J. M., and McDermott, F. (1993). Mantle and slab contributions in arc magmas. *Annu. Rev. Earth Planet. Sci.* 21, 175–204. doi:10.1146/annurev.ea.21.050193.001135

He, H., Li, Y., Wang, C., Zhou, A., Qian, X., Zhang, J., et al. (2018). Late Cretaceous (ca. 95 Ma) magnesian andesites in the Biluoco area, southern Qiangtang subterrane, central Tibet: Petrogenetic and tectonic implications. *Lithos* 302-303, 389–404. doi:10.1016/j.lithos.2018.01.013

Heiken, G., and Eichelberger, J. C. (1980). Eruptions at chaos crags, lassen volcanic national park, California. *J. Volcanol. Geotherm. Res.* 7 (3), 443–481. doi:10.1016/0377-0273(80)90042-6

Hoskin, P. W. O., and Schaltegger., U. (2003). The composition of zircon and igneous and metamorphic petrogenesis. *Rev. Mineralogy Geochem.* 53 (1), 27–62. doi:10.2113/0530027

Hu, W-L., Wang, Q., Tang, G-J., Zhang, X-Z., Qi, Y., Wang, J., et al. (2022). Late early cretaceous magmatic constraints on the timing of closure of the bangong–nujiang tethyan ocean, central tibet. *Lithos* 416-417, 106648. doi:10.1016/j.lithos.2022.106648

Hu, W-L., Wang, Q., Yang, J-H., Zhang, C., Tang, G-J., Lin, M., et al. (2019). Late early Cretaceous peraluminous biotite granites along the Bangong–Nujiang Suture Zone, Central Tibet: Products derived by partial melting of metasedimentary rocks? *Lithos* 344-345, 147–158. doi:10.1016/j.lithos.2019.06.005

Hu, X., Ma, A., Xue, W., Garzanti, E., Cao, Y., Li, S-M., et al. (2022). Exploring a lost ocean in the Tibetan plateau: Birth, growth, and demise of the bangong-nujiang ocean. *Earth-Science Rev.* 229, 104031. doi:10.1016/j.earscirev.2022.104031

Hu, Z., Zhang, W., Liu, Y., Gao, S., Li, M., Zong, K., et al. (2015). Wave" signal-smoothing and mercury-removing device for laser ablation quadrupole and multiple collector ICPMS analysis: Application to lead isotope analysis. *Anal. Chem.* 87 (2), 1152–1157. doi:10.1021/ac503749k

Hu, Z., Liu, Y., Gao, S., Liu, W., Zhang, W., Tong, X., et al. (2012). Improved *in situ* Hf isotope ratio analysis of zircon using newly designed X skimmer cone and jet sample cone in combination with the addition of nitrogen by laser ablation multiple collector ICP-MS. *J. Anal. Atomic Spectrom.* 27 (9), 1391–1399. doi:10.1039/c2ja30078h

Huang, Q-T., Liu, W-L., Xia, B., Cai, Z-R., Chen, W-Y., Li, J-F., et al. (2017). Petrogenesis of the majiari ophiolite (Western tibet, China): Implications for intra-oceanic subduction in the bangong–nujiang tethys. *J. Asian Earth Sci.* 146, 337–351. doi:10.1016/j.jseaes.2017.06.008

Jiang, S., Jiang, Y., Liu, Y., Li, S., Zhang, W., Wang, G., et al. (2021). The bangong-nujiang suture zone, tibet plateau: Its role in the tectonic evolution of the eastern Tethys Ocean. *Earth-Science Rev.* 218, 103656. doi:10.1016/j.earscirev.2021.103656

Jie, L. A., Liu, Y., Yang, Y., and Hu, Z. (2016). Calibration and correction of LA-ICP-MS and LA-MC-ICP-MS analyses for element contents and isotopic ratios. *Solid Earth Sci.* 1 (1), 5–27. doi:10.1016/j.sesci.2016.04.002

Jon, W. H., Janet, H., Shelley, M., Steve, E., and Kemp, R. (2004). Zircon Hf-isotope analysis with an excimer laser, depth profiling, ablation of complex geometries, and concomitant age estimation. *Chem. Geol.* 209, 121–135. doi:10.1016/j.chemgeo.2004.04.026

Kanayama, K., Umino, S., and Ishizuka, O. (2012). Eocene volcanism during the incipient stage of izu-ogasawara arc: Geology and petrology of the mukojima island Group, the ogasawara islands. *Isl. Arc* 21 (4), 288–316. doi:10.1111/iar.12000

Kapp, P., DeCelles, P. G., Gehrels, G. E., Heizler, M., and Ding, L. (2007). Geological records of the lhasa-qiangtang and indo-asian collisions in the Nima area of central tibet. *Geol. Soc. Am. Bull.* 119 (7-8), 917–933. doi:10.1130/b26033.1

Kapp, P., Yin, A., Harrison, T. M., and Ding, L. (2005). Cretaceous-Tertiary shortening, basin development, and volcanism in central Tibet. *Bull. Geol. Soc. Am.* 117 (7-8), 865–878. doi:10.1130/B25595.1

Kuno, H. (1968). Origin of andesite and its bearing on the Island arc structure. *Bull. Volcanol.* 32 (1), 141–176. doi:10.1007/BF02596589

La Flèche, M. R., Camiré, G., and Jenner, G. A. (1998). Geochemistry of post-acadian, carboniferous continental intraplate basalts from the maritimes basin, magdalen islands, québec, Canada. *Chem. Geol.* 148 (3), 115–136. doi:10.1016/S0009-2541(98)00002-3

Li, C., Zeng, M., Li, Z., and Chen, S. (2020). Origin and tectonic implications of late jurassic high-Mg diorites along the bangong-nujiang suture zone, tibet. *Int. Geol. Rev.* 63 (11), 1406–1422. doi:10.1080/00206814.2020.1768444

Li, C-F., Li, X-H., Li, Q-L., Guo, J-H., Li, X-H., and Yang, Y-H. (2012). Rapid and precise determination of Sr and Nd isotopic ratios in geological samples from the same filament loading by thermal ionization mass spectrometry employing a single-step separation scheme. *Anal. Chim. Acta* 727 (10), 54–60. doi:10.1016/j.aca.2012.03.040

Li, D., Wang, G. H., Bons, P. D., Zhao, Z. B., Du, J. X., Wang, S. L., et al. (2020). Subduction reversal in a divergent double subduction zone drives the exhumation of southern Qiangtang blueschist-bearing melange, central tibet. *TECTONICS* 39 (4). doi:10.1029/2019TC006051

Li, H-Q., Li, T-F., He, Z-Y., and Ji, F-B. (2022). Early Cretaceous hydrous mafic magmatism in the eastern Lhasa Terrane, Tibet: Petrogenesis and constraints on the early history of the eastern Jiali (Parlung) fault. *Lithos* 418-419, 106686. doi:10.1016/j.lithos.2022.106686

Li, J-X., Qin, K-Z., Li, G-M., Richards, J. P., Zhao, J-X., and Cao, M-J. (2014). Geochronology, geochemistry, and zircon Hf isotopic compositions of Mesozoic intermediate–felsic intrusions in central Tibet: Petrogenetic and tectonic implications. *Lithos* 198-199, 77–91. doi:10.1016/j.lithos.2014.03.025

Li, J-X., Qin, K-Z., Li, G-M., Xiao, B., Zhao, J-X., and Chen, L. (2016). Petrogenesis of cretaceous igneous rocks from the duolong porphyry Cu-Au deposit, central tibet: Evidence from zircon U-Pb geochronology, petrochemistry and Sr-Nd-Pb-Hf isotope characteristics. *Geol. J.* 51 (2), 285–307. doi:10.1002/gj.2631

Li, S-M., Zhu, D-C., Wang, Q., Zhao, Z., Zhang, L-L., Liu, S-A., et al. (2016). Slab-derived adakites and subslab asthenosphere-derived OIB-type rocks at 156 ± 2 Ma from the north of Gerze, central Tibet: Records of the Bangong–Nujiang oceanic ridge subduction during the Late Jurassic. *Lithos* 262, 456–469. doi:10.1016/j.lithos.2016.07.029

Li, S-M., Zhu, D-C., Wang, Q., Zhao, Z-D., Sui, Q-L., Liu, S-A., et al. (2014). Northward subduction of bangong–nujiang tethys: Insight from late jurassic intrusive rocks from Bangong Tso in Western tibet. *Lithos* 205, 284–297. doi:10.1016/j.lithos.2014.07.010

Li, S. M., Wang, Q., Zhu, D. C., Stern, R. J., Cawood, P. A., Sui, Q. L., et al. (2018). One or two early cretaceous arc systems in the Lhasa terrane, southern tibet. *J. Geophys. Res. Solid Earth* 123 (5), 3391–3413. doi:10.1002/2018jb015582

Li, X-K., Chen, J., Wang, R-C., Cai, L., Wang, M., Liu, J-H., et al. (2019). Early cretaceous tectonomagmatic evolution and basin development of Western bangong–nujiang suture: A complete history of soft collision. *Lithos* 344-345, 360–373. doi:10.1016/j.lithos.2019.06.030

Li, X. K., Chen, J., Wang, R. C., and Li, C. (2018). Temporal and spatial variations of Late Mesozoic granitoids in the SW Qiangtang, Tibet: Implications for crustal architecture, Meso-Tethyan evolution and regional mineralization. *EARTH-SCIENCE Rev.* 185, 374–396. doi:10.1016/j.earscirev.2018.04.005

Li, X., Wang, B., Liu, H., Wang, L., Chen, L., Yan, G., et al. (2017). Petrogenesis of early jurassic volcanic rocks in the amdo area, tibet: Evidences for the subduction of the Bangong-Nujiang Tethys ocean. *Yanshi Xuebao/Acta Petrol. Sin.* 33 (7), 2073–2084.

Li, Y., He, J., Wang, C., Han, Z., Ma, P., Xu, M., et al. (2015a). cretaceous volcanic rocks in South Qiangtang terrane: Products of northward subduction of the bangong-nujiang ocean? *J. ASIAN EARTH Sci.* 104:69–83. doi:10.1016/j.jseaes.2014.09.033

Li, Y., Wang, G., Santosh, M., Wang, J. F., Dong, P., and Li, H. (2018). Supra-subduction zone ophiolites from inner Mongolia, north China: Implications for the tectonic history of the southeastern central asian orogenic belt. *Gondwana Res.* 59, 126–143. doi:10.1016/j.gr.2018.02.018

Li, Y. J., Wang, G., Santosh, M., Wang, J. F., Dong, P., and Li, H. Y. (2020). Subduction initiation of the SE Paleo-Asian Ocean: Evidence from a well preserved intra-oceanic forearc ophiolite fragment in central Inner Mongolia, North China. *Earth Planet. Sci. Lett.* 535, 116087. doi:10.1016/j.epsl.2020.116087

Li, Y. J., Wang, J. F., Li, H. Y., Liu, Y. C., Dong, P. P., Liu, D. W., et al. (2012). Recognition of diyanmiao ophiolite in xi U jimqin banner, inner Mongolia. *Acta Petrol. Sin.* 28 (4), 1282–1290. (in Chinese with English abstract).

Liu, H. C., Huang, Q., Uysal, I. T., Cai, Z., Wan, Z., Xia, B., et al. (2020). Geodynamics of the divergent double subduction along the Bangong-Nujiang tethyan Suture Zone: Insights from late mesozoic intermediate-mafic rocks in central Tibet. *Gondwana Res.* 79, 233–247. doi:10.1016/j.gr.2019.09.018

Liu, W-L., Xia, B., Zhong, Y., Cai, J-X., Li, J-F., Liu, H-F., et al. (2014). Age and composition of the rebang Co and julu ophiolites, central tibet: Implications for the evolution of the Bangong meso-tethys. *Int. Geol. Rev.* 56 (4), 430–447. doi:10.1080/00206814.2013.873356

Liu, Y., Li, S., Xie, C., Santosh, M., Liu, Y., Dong, Y., et al. (2022). Subduction–collision and exhumation of eclogites in the Lhasa terrane, tibet plateau. *Gondwana Res.* 102, 394–404. doi:10.1016/j.gr.2020.01.019

Liu, Y., Tan, J., Wei, J., Zhao, S., Liu, X., Gan, J., et al. (2019). Sources and petrogenesis of late triassic zhiduo volcanics in the northeast tibet: Implications for tectonic evolution of the Western Jinsha paleo-tethys ocean. *Lithos* 336-337, 169–182. doi:10.1016/j.lithos.2019.04.005

Liu, Y., Gao, S., Hu, Z., Gao, C., Zong, K., and Wang, D. (2010a). Continental and oceanic crust recycling-induced melt–peridotite interactions in the trans-north China orogen: U–Pb dating, Hf isotopes and trace elements in zircons from mantle xenoliths. *J. Petrology* 51 (1-2), 537–571. doi:10.1093/petrology/egp082

Liu, Y. S., Gao, S., Hu, Z. C., Gao, C., Zong, K., and Wang, D. (2010b). Continental and oceanic crust recycling-induced melt-peridotite interactions in the trans-north China orogen: U-Pb dating, Hf isotopes and trace elements in zircons from mantle xenoliths. *J. PETROLOGY* 51 (1-2), 537–571. doi:10.1093/petrology/egp082

Liu, Y. S., Hu, Z., Gao, S., Günther, D., Xu, J., Gao, C., et al. (2008). *In situ* analysis of major and trace elements of anhydrous minerals by LA-ICP-MS without applying an internal standard. *Chem. Geol.* 257 (1), 34–43. doi:10.1016/j.chemgeo.2008.08.004

Ludwig, K. R. (2003). *Isoplot 3.0: A geochronological toolkit for microsoft excel*. California: Berkeley Geochronology Center Special Publication.

Luo, A-B., Fan, J-J., Zhang, B-C., and Hao, Y-J. (2022b). Cretaceous uplift history of the Tibetan Plateau: Insights from the transition of marine to terrestrial facies in central Tibet. *Palaeogeogr. Palaeoclimatol. Palaeoecol.* 601, 111103. doi:10.1016/j.palaeo.2022.111103

Luo, A. B., Fan, J. J., Sun, D. Y., Wu, H., Yu, Y. P., Zhang, B. C., et al. (2022a). Terminal stage of divergent double subduction: Insights from Early Cretaceous magmatic rocks in the Gerze area, central Tibet. *LITHOS* 420, 106713. doi:10.1016/j.lithos.2022.106713

Ma, X., Song, Y., Tang, J., and Chen, W. (2020). Newly identified rhyolite-biotite monzogranite (A2-type granite)-norite belt from the Bangong-Nujiang collision zone in Tibet Plateau: Evidence for the slab break-off beneath the Lhasa Terrane. *Lithos* 366-367, 105565. doi:10.1016/j.lithos.2020.105565

Marschall, H. R., and Schumacher, J. C. (2012). Arc magmas sourced from melange diapirs in subduction zones. *Nat. Geosci.* 5 (12), 862–867. doi:10.1038/NGEO1634

Parman, S. W., and Grove, T. L. (2004). Harzburgite melting with and without H2O: Experimental data and predictive modeling. *J. Geophys. Research-Solid Earth* 109 (B2). doi:10.1029/2003JB002566

Pearce, J. A. (2008). Geochemical fingerprinting of oceanic basalts with applications to ophiolite classification and the search for Archean oceanic crust. *Lithos* 100 (1), 14–48. doi:10.1016/j.lithos.2007.06.016

Pearce, J. A., and Parkinson, I. J. (1993). Trace element models for mantle melting: Application to volcanic arc petrogenesis. *Magmatic Process. plate Tect.* 76, 373–403. doi:10.1144/gsl.sp.1993.076.01.19

Pearce, J. A., and Peate, D. W. (1995). Tectonic implications of the composition of volcanic arc magmas. *Annu. Rev. Earth Planet. Sci.* 23, 251–285. doi:10.1146/annurev.ea.23.050195.001343

Pei, Q-M., Zhang, S-T., Hayashi, K-I., Cao, H-W., Dong, L., Tang, L., et al. (2018). Permo-triassic granitoids of the xing'an-Mongolia segment of the central asian orogenic belt, northeast China: Age, composition, and tectonic implications. *Int. Geol. Rev.* 60 (9), 1172–1194. doi:10.1080/00206814.2017.1377121

Peng, Y., Yu, S., Li, S., Liu, Y., Santosh, M., Lv, P., et al. (2020). The odyssey of Tibetan Plateau accretion prior to Cenozoic India-Asia collision: Probing the Mesozoic tectonic evolution of the Bangong-Nujiang Suture. *Earth-Science Rev.* 211, 103376. doi:10.1016/j.earscirev.2020.103376

Perez, A., Umino, S., Yumul, G. P., Jr., and Ishizuka., O. (2018). Boninite and boninite-series volcanics in northern zambales ophiolite: Doubly vergent subduction initiation along philippine sea plate margins. *Solid earth.* 9 (3), 713–733. doi:10.5194/se-9-713-2018

Perugini, D., and Poli, G. (2012). The mixing of magmas in plutonic and volcanic environments: Analogies and differences. *Lithos* 153, 261–277. doi:10.1016/j.lithos.2012.02.002

Pin, C., and Paquette, J. L. (1997). A mantle-derived bimodal suite in the hercynian belt: Nd isotope and trace element evidence for a subduction-related rift origin of the late devonian Brévenne metavolcanics, massif central (France). *Contributions Mineralogy Petrology* 129 (2-3), 222–238. doi:10.1007/s004100050334

Ran, H., Wang, G., Liang, X., Zheng, Y., and Jiumi, D. (2015). The late jurassic diorite in rongma area, southern Qiangtang terrane, Tibetan plateau: Product of northward subduction of the Bangong Co-nujiang river Tethys Ocean. *Geol. Bull. China* 34 (5), 815–825.

Rapp, R. P., and Bruce Watson, E. (1995). Dehydration melting of metabasalt at 8–32 kbar: Implications for continental growth and crust-mantle recycling. *J. Petrology* 36 (4), 891–931. doi:10.1093/petrology/36.4.891

Rehkamper, M., and Hofmann, A. W. (1997). Recycled ocean crust and sediment in Indian Ocean MORB. *Earth And Planet. Sci. Lett.* 147 (1-4), 93–106. doi:10.1016/S0012-821X(97)00009-5

Roberts, M. P., and Clemens, J. D. (1993). Origin of high-potassium, talc-alkaline, I-type granitoids. *Geology* 21 (9), 825–828. doi:10.1130/0091-7613(1993)021<0825:oohpta>2.3.co;2

Russell, W. A., Papanastassiou, D. A., and Tombrello, T. A. (1978). Ca isotope fractionation on the Earth and other solar system materials. *Geochimica Cosmochimica Acta* 42, 1075–1090. doi:10.1016/0016-7037(78)90105-9

Shi, Z. X., Gao, R., Lu, Z. W., Li, W. H., Li, H. Q., Huang, X. F., et al. (2022). Bidirectional subduction of the Bangong-Nujiang ocean revealed by deep-crustal seismic reflection profile. *Tectonophysics* 837, 229455. doi:10.1016/j.tecto.2022.229455

Sisson, T. W., and Grove, T. L. (1993). Experimental investigations of the role of H2O in calc-alkaline differentiation and subduction zone magmatism. *Contributions Mineralogy Petrology* 113 (2), 143–166. doi:10.1007/BF00283225

Soesoo, A., Bons, P. D., Gray, D. R., and Foster, D. A. (1997). Divergent double subduction: Tectonic and petrologic consequences. *Geology* 25, 755–758. doi:10.1130/0091-7613(1997)025<0755:DDSTAP>2.3.CO;2

Sui, Q-L., Wang, Q., Zhu, D. C., Zhao, Z. D., Chen, Y., Santosh, M., et al. (2013). Compositional diversity of ca. 110Ma magmatism in the northern Lhasa Terrane, Tibet Implications for the magmatic origin and crustal growth in a continent–continent collision zone. *Lithos* 168-169, 144–159. doi:10.1016/j.lithos.2013.01.012

Sun, S.-s., and McDonough, W. F. (1989). Chemical and isotopic systematics of oceanic basalts: Implications for mantle composition and processes. *Geol. Soc. Lond. Spec. Publ.* 42 (1), 313–345. doi:10.1144/gsl.sp.1989.042.01.19

Tang, Y., Zhai, Q., Hu, P., Xiao, X., and Wang, H. (2018). Petrology, geochemistry and geochronology of the zhongcang ophiolite, northern tibet: Implications for the evolution of the bangong-nujiang ocean. *Geosci. Front.* 9 (5), 1369–1381. doi:10.1016/j.gsf.2018.05.007

Tatsumi, Y. (1982). Origin of high-magnesian andesites in the Setouchi volcanic belt, southwest Japan, II. Melting phase relations at high pressures. *Earth Planet. Sci. Lett.* 60 (2), 305–317. doi:10.1016/0012-821X(82)90009-7

Tepper, J. H., Nelson, B. K., Bergantz, G. W., and Irving, A. J. (1993). Petrology of the chilliwack batholith, north cascades, Washington - generation of calc-alkaline granitoids by melting of mafic lower crust with variable water fugacity. *Contributions Mineralogy And Petrology* 113 (3), 333–351. doi:10.1007/BF00286926

Tong, X., Yan, J. J., Zhao, Z., Niu, Y., Qi, N., Shi, Q., et al. (2022). Middle-Late Jurassic magmatism in the west central Lhasa subterrane, Tibet: Petrology, zircon chronology, elemental and Sr-Nd-Pb-Hf-Mg isotopic geochemistry. *Lithos* 408-409, 106549. doi:10.1016/j.lithos.2021.106549

Tsuchiya, N., Suzuki, S., Kimura, J-I., and Kagami, H. (2005). Evidence for slab melt/mantle reaction: Petrogenesis of early cretaceous and eocene high-Mg andesites from the kitakami mountains, Japan. *Lithos* 79 (1), 179–206. doi:10.1016/j.lithos.2004.04.053

Wang, B-D., Wang, L-Q., Chung, S-L., Chen, J-L., Yin, F-G., Han, L., et al. (2016). Evolution of the Bangong–Nujiang Tethyan ocean: Insights from the geochronology and geochemistry of mafic rocks within ophiolites. *Lithos* 245, 18–33. doi:10.1016/j.lithos.2015.07.016

Wang, K., and Wright, J. (1987). Architecture of sarcomere matrix in skeletal muscle. Evidence that nebulin constitutes a distinct set of non-extensible filaments in parallel with titin filaments. *J. Cell Biol.* 105, 138.

Wang, W., Zhai, Q-G., Hu, P-Y., Chung, S-L., Tang, Y., Wang, H-T., et al. (2020). Late cretaceous adakitic rocks from the Western Tibetan plateau: Implications for the subduction of the neo-tethys ocean. *Int. Geol. Rev.* 63 (15), 1884–1899. doi:10.1080/00206814.2020.1805803

Wang, Z-L., Fan, J-J., Wang, Q., Hu, W-L., Yang, Z-Y., and Wang, J. (2021). Reworking of juvenile crust beneath the bangong–nujiang suture zone: Evidence from late cretaceous granite porphyries in southern Qiangtang, central tibet. *Lithos* 390-391, 106097. doi:10.1016/j.lithos.2021.106097

Wei, S-G., Tang, J-X., Song, Y., Liu, Z-B., Feng, J., and Li, Y-B. (2017). Early Cretaceous bimodal volcanism in the Duolong Cu mining district, Western Tibet: Record of slab breakoff that triggered ca. 108–113 Ma magmatism in the Western Qiangtang Terrane. *J. Asian Earth Sci.* 138, 588–607. doi:10.1016/j.jseaes.2016.12.010

Woodhead, J. D., Hergt, J. M., Davidson, J. P., and Eggins, S. M. (2001). Hafnium isotope evidence for 'conservative' element mobility during subduction zone processes. *Earth Planet. Sci. Lett.* 192 (3), 331–346. doi:10.1016/S0012-821X(01)00453-8

Wu, F. Y., Li, X. H., Zheng, Y. F., and Gao, S. (2007). Lu-Hf isotopic systematics and their applications in petrology. *Acta Petrol. Sin.* 23 (2), 185–220.

Xu, W., Cai, L., Wang, M., Fan, J-J., Wu, H., and Li, X. (2017). Subduction of a spreading ridge within the Bangong Co–nujiang Tethys Ocean: Evidence from early cretaceous mafic dykes in the duolong porphyry Cu–Au deposit, Western tibet. *Gondwana Res.* 41, 128–141. doi:10.1016/j.gr.2015.09.010

Yan, L-L., and Zhang, K-J. (2020). Infant intra-oceanic arc magmatism due to initial subduction induced by oceanic plateau accretion: A case study of the Bangong meso-tethys, central tibet, Western China. *Gondwana Res.* 79, 110–124. doi:10.1016/j.gr.2019.08.008

Yang, J-H., Sun, J-F., Zhang, J-H., and Wilde, S. A. (2012). Petrogenesis of Late Triassic intrusive rocks in the northern Liaodong Peninsula related to decratonization of the North China Craton: Zircon U–Pb age and Hf–O isotope evidence. *Lithos* 153, 108–128. doi:10.1016/j.lithos.2012.06.023

Yang, Z., Tang, J., Zhang, K., Zhao, X., Li, H., Wang, Y., et al. (2021). Southward subduction of the Bangong–Nujiang oceanic lithosphere triggered back-arc spreading: Evidence from the Late Jurassic Kongnongla magnesian andesites in central Tibet. *Lithos* 398-399, 106250. doi:10.1016/j.lithos.2021.106250

Yang, Z-Y., Wang, Q., Zhang, C., Yang, J. H., Ma, L., Wang, J., et al. (2019). Cretaceous (~100 Ma) high-silica granites in the gajin area, central tibet: Petrogenesis and implications for collision between the Lhasa and Qiangtang terranes. *Lithos* 324-325, 402–417. doi:10.1016/j.lithos.2018.11.011

Yin, A., and Harrison, T. M. (2000). Geologic evolution of the Himalayan-Tibetan orogen. *Annu. Rev. Earth Planet. Sci.* 28, 211–280. doi:10.1146/annurev.earth.28.1.211

Zhang, J., Fan, W., Peng, T., and Ratschbacher, L. (2022). An Early Cretaceous arc–back-arc system in Western Yunnan, SW China: Constraints from U Pb zircon ages and geochemistry of volcanic rocks in the Western Baoshan block. *Lithos* 422-423, 106753. doi:10.1016/j.lithos.2022.106753

Zhang, J., Fan, W., Peng, T., and Ratschbacher, L. (2021). Southeastern continuation of the bangong-nujiang suture zone: Constraints from middle jurassic–early cretaceous sedimentary rocks in the Western baoshan block, SW China. *J. Asian Earth Sci.* 221, 104944. doi:10.1016/j.jseaes.2021.104944

Zhang, Q., Guo, F., Zhao, L., and Wu, Y. (2017). Geodynamics of divergent double subduction: 3-D numerical modeling of a cenozoic example in the molucca sea region, Indonesia. *J. Geophys. Research-Solid Earth* 122 (5), 3977–3998. doi:10.1002/2017JB013991

Zhang, W., Hu, Z., and Liu, Y. (2020). Iso-compass: New freeware software for isotopic data reduction of LA-MC-ICP-MS. *J. Anal. Atomic Spectrom.* 35, 1087–1096. doi:10.1039/d0ja00084a

Zhao, B., Shi, R-D., Zou, H-B., Chen, S-S., Huang, Q-S., Sun, Y-L., et al. (2021). Intra-continental boninite-series volcanic rocks from the bangong-nujiang suture zone, central tibet. *Lithos* 386-387, 106024. doi:10.1016/j.lithos.2021.106024

Zhao, G. (2015). Jiangnan orogen in South China: Developing from divergent double subduction. *Gondwana Res.* 27 (3), 1173–1180. doi:10.1016/j.gr.2014.09.004

Zhao, R., Yan, Q., Zhang, H., Guan, Y., Ge, Z., Yuan, L., et al. (2020). The chemical composition of global subducting sediments and its geological significance. *Adv. Earth Sci.* 35 (8), 789–803.

Zheng, Y. F., Chen, Y. X., Dai, L. Q., and Zhao, Z. F. (2015). Developing plate tectonics theory from oceanic subduction zones to collisional orogens. *Sci. China-Earth Sci.* 58 (7), 1045–1069. doi:10.1007/s11430-015-5097-3

Zhong, Y., Liu, W-L., Xia, B., Liu, J-N., Guan, Y., Yin, Z-X., et al. (2017). Geochemistry and geochronology of the Mesozoic Lanong ophiolitic mélange, northern Tibet: Implications for petrogenesis and tectonic evolution. *Lithos* 292-293, 111–131. doi:10.1016/j.lithos.2017.09.003

Zhu, D-C., Li, S-M., Cawood, P. A., Wang, Q., Zhao, Z-D., Liu, S-A., et al. (2016). Assembly of the Lhasa and Qiangtang terranes in central Tibet by divergent double subduction. *Lithos* 245, 7–17. doi:10.1016/j.lithos.2015.06.023

Zhu, D-C., Zhao, Z-D., Niu, Y., Dilek, Y., Hou, Z-Q., and Mo, X-X. (2013). The origin and pre-Cenozoic evolution of the Tibetan Plateau. *Gondwana Res.* 23 (4), 1429–1454. doi:10.1016/j.gr.2012.02.002

Zhu, D-C., Zhao, Z-D., Niu, Y., Dilek, Y., Wang, Q., Ji, W-H., et al. (2012). Cambrian bimodal volcanism in the Lhasa Terrane, southern Tibet: Record of an early Paleozoic Andean-type magmatic arc in the Australian proto-Tethyan margin. *Chem. Geol.* 328, 290–308. doi:10.1016/j.chemgeo.2011.12.024

Zhu, D-C., Zhao, Z. D., Niu, Y., Mo, X. X., Chung, S. L., Hou, Z. Q., et al. (2011). The Lhasa Terrane: Record of a microcontinent and its histories of drift and growth. *Earth Planet. ence Lett.* 301, 241–255. doi:10.1016/j.epsl.2010.11.005

Zhu, D., Pan, G., Mo, X., Liao, Z., Jiang, X., Wang, L., et al. (2007). Petrogenesis of volcanic rocks in the sangxiu formation, central segment of tethyan Himalaya: A probable example of plume-lithosphere interaction. *J. Asian Earth Sci.* 29 (2-3), 320–335. doi:10.1016/j.jseaes.2005.12.004

Zong, K., Klemd, R., Yuan, Y., He, Z., Guo, J. L., Shi, X., et al. (2017). The assembly of Rodinia: The correlation of early Neoproterozoic (ca. 900Ma) high-grade metamorphism and continental arc formation in the southern Beishan Orogen, southern Central Asian Orogenic Belt (CAOB). *Precambrian Res.* 290, 32–48. doi:10.1016/j.precamres.2016.12.010